Journal of Solid State Chemistry 184 (2011) 3028–3033

Contents lists available at SciVerse ScienceDirect

Journal of Solid State Chemistry

journal homepage: www.elsevier.com/locate/jssc

Raman and structural characterization of $LuAlO_3$

Alberto Casu [a,b,*], Pier Carlo Ricci [a]

[a] Dipartimento di Fisica, Università di Cagliari—S.P. Monserrato-Sestu Km 0.700 09042 Monserrato, Cagliari, Italy
[b] Istituto Italiano di Tecnologia, Via Morego n. 30 16163 Genova, Italy

ARTICLE INFO

Article history:
Received 30 June 2011
Received in revised form
8 September 2011
Accepted 11 September 2011
Available online 17 September 2011

Keywords:
Raman
Pervoskite
$LuAlO_3$
LuAP
EXAFS

ABSTRACT

The structural and vibrational properties of lutetium orthoaluminate perovskite ($LuAlO_3$) were investigated by means of Raman spectroscopy and EXAFS measurements.

The analysis of Raman spectra taken in four different polarized configurations along the principal axes at 20 K and room temperature conditions permits to assign the principal vibrational modes in LuAP single crystals and to confirm the belonging to the D_{2h}^{16} space group.

EXAFS measurements were performed at room temperature in order to obtain local structural informations on the first and next nearest neighbors around lutetium absorptions sites. Unit cell parameters and bond lengths were determined by the analysis of the EXAFS spectroscopy at the L_3 absorption edge of lutetium.

The informations thus gathered on this compound can offer a useful addition in the framework of a full structural characterization of $LuAlO_3$.

1. Introduction

Cerium-doped lutetium aluminum perovskite $LuAlO_3$ (LuAP) has been widely known for a number of years as a good candidate for scintillator applications due to its characteristics of high light yield (10,000 ph/MeV), high crystal density ($\sim$8.0 g/cm^3) and short decay time (about 20 ns) [1]. Despite these features, the diffusion of Ce:LuAP crystals was slowed down by practical difficulties in the growth process of single crystals, such as the necessity of high temperatures for the melt and the choice of parameters during the pulling process; moreover, typical macroscopic defects like solid and gaseous inclusions, twin boundaries and cracks can strongly affect the performance of LuAP based scintillator devices. A second but not marginal drawback is linked to the high cost of pure starting oxides, mainly the Lu_2O_3. In this regard a mixed lutetium/yttrium perovskite was subsequently developed. The coupling of these different problems, each of whom could have been overcome by itself, prevented a wide diffusion of LuAP up to recent times. As a consequence, although the material cannot be labeled as completely new [2] and the first single-phase LuAP crystals were made available in the middle of 1990s [3], it has been put aside for a long time and even in recent times the majority of literature works was devoted towards studies with an immediate applicative effect [4–9], while a full structural characterization is still missing.

The aim of the present work is to fill this void by means of a joint approach involving Raman and Extended X-Ray Absorption Fine Structure (EXAFS) spectroscopies: the first method will offer a complete analysis of the vibrational modes of LuAP crystals by means of polarized Raman spectroscopy in the temperature range of 20–290 K, while EXFAS spectroscopy will give informations of both local and general on the structural characteristics. Besides the importance of knowing the basis properties, a deep characterization of the structure of LuAP single crystals can strongly improve the development of Cerium doped LuAP scintillators.

2. Experimental techniques and analytical principles

LuAP samples of different commercial origins grown by the Czochralski method were studied. Raman spectra were acquired from single monocrystals in backscattering geometry along the principal crystal directions and from crystalline powder using the 488.0 nm line of an argon ion laser. The samples were mounted in an LTS-22-C-330 Workhorse-type optical cryogenic system for low temperature measurements. Spectra were acquired with a triple spectrometer Jobin–Yvon Dilor integrated system with a spectral resolution of about 1 cm^{-1} and by a 1200 grooves/mm grating monochromator and a CCD detector system. Porto's notation was used to describe the scattering geometry [10].

EXAFS data were collected at the XAFS beamline of the Elettra synchrotron facility in Trieste (Italy). Data were recorded in

* Corresponding author at: Università di Cagliari—Dipartimento di Fisica, S.P. Monserrato-Sestu Km, 0.700 09042, Monserrato, Cagliari, Italy.
E-mail address: alberto.casu@iit.it (A. Casu).

0022-4596/$ - see front matter © 2011 Elsevier Inc. All rights reserved.
doi:10.1016/j.jssc.2011.09.007

transmission mode with an average beam current of 120 mA (multibunch) and a working energy of 2.4 GeV. All the ionization chambers were kept at a total pressure of 2 bars by filling them with appropriate gas mixtures of He, N_2, Ar and Kr for the absorption edge of choice (the L_3 edge of lutetium, 9244 eV with a relative energy resolution of 2×10^{-4}). The presented data are averaged over 3 cycles of collection and are relative to pellets composed by a mixture of nanopowder crystals and polivinilpirrolidone (PVP), used to improve their stability. The resulting data were weighted by k^2 and fitted in R space in the range 1.1–4.0 Å (k-range being 2.0–11.6 $Å^{-1}$) using the IFEFFIT suite of programs [11,12].

The basis of the fitting process for EXAFS data is given by the so called EXAFS equation, where $\chi(k)$ indicates the sum of oscillatory signals arising from scattering processes involving photoelectrons ejected from the X-ray absorbing atom, scattering from its neighbors of different shells and returning back to the starting point. The general structure of the EXAFS equation allows to distinguish between an amplitude term (dependent on atomic number of the scattering atom and on the coordination number of the shells) and a phase term (dependent on distance R of the photo-absorber's coordination sphere), so that $\chi(k)$ can be expressed as

$$\chi(k)=\sum_j \frac{N_j S_0^2 f_j(k) e^{(-2R_j/\lambda(k)} e^{(-2)k^2\sigma_j^2}}{kR_j^2}\sin\left[2kR_j+\delta_j(k)\right] \quad (1)$$

where N is the coordination number of neighboring atoms, S_0^2 is the amplitude reduction term, $f(k)$ is the scattering amplitude, $\delta(k)$ is the phase-shift, σ^2 is the mean-square disorder of neighbor distance and R is the distance to neighboring atoms.

Fitting of EXAFS data was achieved using the first fifteen scattering paths from a theoretical crystalline structure calculated by IFEFFIT, them being single scattering paths between the central atom and all the atoms of the unit cell plus the ones relative to the next-nearest lanthanide ions. Among these paths three different shells can be distinguished: a first shell of oxygens, a second one featuring both oxygen and aluminum atoms, and a final shell featuring the first six lutetium neighbors (radially divided in three couples: one along the Z axis and two in the horizontal plane). The fitting parameters were consequently chosen in order to take into account the presence of different chemical elements in different shells, while always keeping their total number well below the number of independent data points. Fig. 1A reports a sketch of the atoms featured in each shell.

The goodness of the fitting results was given by a parameter measuring the absolute misfit between theory and data, called

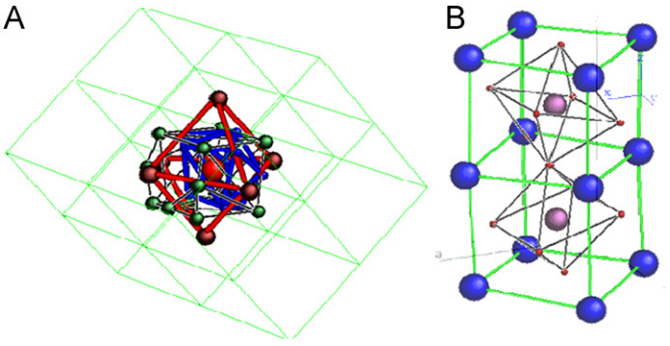

Fig. 1. (A) Sketch of the shells used during the fitting of EXAFS data of $LuAlO_3$ (different colors are used for different shells, not for different chemical elements) and (B) sketch of the unit cell of a Pbnm R.E.AlO_3 crystal (blue spheres stand for Rare Earth ions, purple spheres for aluminium ions and red spheres for oxygen ions). (For interpretation of the references to color in this figure legend, the reader is referred to the web version of this article.)

R-factor, which can be expressed by the formula

$$R=\sum_i \frac{[\Im m(\chi_{dat}(R_i)-\chi_{th}(R_i))]^2+[\Re e(\chi_{dat}(R_i)-\chi_{th}(R_i))]^2}{[\Im m(\chi_{dat}(R_i))]^2+[\Re e(\chi_{dat}(R_i))]^2} \quad (2)$$

Since the fitting procedures of EXAFS data by IFEFFIT are based on the tailoring of a user-defined theoretical crystal against experimental data, a brief introduction on the main characteristics of $LuAlO_3$ should prove useful in order to better comprehend the starting points of the analysis.

Lutetium aluminum perovskite is an orthorhombic perovskite of the D_{2h}^{16} space group, featuring a 20 atoms unit cell, and belongs to the family of rotationally distorted perovskites with Glazer's notation ($a^-b^+a^-$).

The general structure of perovskite crystals can be expressed as **ABX**$_3$, where elements **A** and **B** occupy, respectively, the vertexes and the central site of the body centered cube, while **X** anions, situated on the six faces of the cube, form an octahedron around the central site B.

In particular, **B** cations are coordinated by six **X** anions (forming an octahedron), while **A** cations are coordinated by 12 anions (forming a cuboctahedron). **X** anions (generally represented by oxygens) have coordination number 2 and are coordinated by two **B** cations, since the A–**O** distance is about 40%, larger than the **B**–**O** bond distance. Actually, "**A**" and "**B**" are two cations of very different sizes and in general the larger **A** atom is the main cause of the overall size of the **AO**$_3$ (*fcc*) structure. If we look at the unit cell of $LuAlO_3$ with *Pbnm* structure in Fig. 1B, it is possible to see the presence of a network of cornersharing AlO_6 octahedra, while the A and B sites of the generic cell are occupied, respectively, by lutetium and aluminum ions.

The formation of an orthorhombic structure over the theoretical cubic one can be expected from purely chemical considerations. A perfect perovskite structure **ABX**$_3$ respects the relation

$$a=\sqrt{2}(R_A+R_X)=2(R_B+R_X), \quad (3)$$

where a indicates the cubic cell parameter and R_A, R_B and R_X indicate the ionic radii of its constituting elements. A compound whose chemical elements ionic radii do not satisfy relation (3) can still present a perovskite structure, albeit distorted. On this basis, a tolerance factor t was first proposed by Goldschmidt and defined as

$$t=\frac{R_A+R_X}{\sqrt{2}(R_B+R_X)} \quad (4)$$

A cubic perovskite, whose elements radii respect relation (3), has a tolerance factor value of 1, while the introduction of elements with increased or decreased ionic radii in respect to the cubic condition will result in t parameters higher or lower than the unit value. From a structural point of view variations in t factor hint at the formation of different structures: while t values larger than 1 correspond to the formation of $BaNiO_3$-type structures with face-sharing octahedra, t values higher than 0.80 correspond to the formation of perovskite structures. Obviously perovskite structures with t factors in the range 0.80–1.00 have different structural characteristics, as the decrease in size of the **A** ion correspond to a variation in cell dimensions and a tilt of **BX**$_6$ octahedra in order to fill space, thus lowering the symmetry of the crystal: in particular **ABX**$_3$ crystals with t factors going from 1 to 0.89 still keep a cubic or semicubic structure [13,14], while compounds with lower t factors (down to 0.80) present perovskite structures with an increased octahedra tilting and a inhomogeneous variation of cell parameters that results in the passage from semicubic to orthorhombic crystals. Obviously the choice of correct ionic radii plays a focal role in the calculation of tolerance factors, thus the t parameter was generally used as a rough estimate of perovskites. However in recent times the works of

Jiang et al. [15], Moreira and Dias [16] and Ubic [17] offered more precise, albeit empirical, estimation of perovskite cell parameters based on ionic radii. In light of these facts and taking into account the work Reaney and Iddles [18], the value of t factor for $LuAlO_3$ can be calculated as $t=0.95$ (tolerance factor for YAP is $t=0.96$) [19] and the crystal can be expected to be as a slightly distorted orthorhombic perovskite, which will be starting point of the structural analysis by EXAFS spectroscopy.

Aside from these considerations, based on experimental data, the aforementioned structure can be obtained from the simple perovskite structure by two consequent rotations of AlO_6 octahedra, namely, (1) around the [010] direction of cubic perovskite (the y axis in *Pnma* or the z axis in *Pbnm*); (2) around the [101] direction of cubic perovskite (the x axis in *Pnma* or the y axis in *Pbnm*) [20]. The irreducible point representations of this symmetry group allows 24 Raman active vibrational modes (on a total of 60) [21]:

$$\Gamma = 7A_{1g}+7B_{1g}+5B_{2g}+5B_{3g}+8A_{1u}+8B_{1u}+10B_{2u}+10B_{3u}$$

Raman active modes are $7A_{1g}$ modes, $7B_{1g}$ modes, $5B_{2g}$ modes and $5B_{3g}$ modes and each of these vibrational modes can be assigned to different atomic motions, although not all of them were shown by our measurements.

3. Results and discussion

3.1. Raman measurements

The unpolarized Raman spectra of powder samples recorded at ambient pressure show several bands in the 100–600 cm^{-1} spectral range, some of which are not resolved and/or overlapped, thus not allowing a clear identification of the different vibrational modes (Fig. 2). This problem led to the choice of acquiring differently-polarized Raman spectra of single crystals along its three main axes in order to show the Raman active modes [22,23].

For a crystal in a D_{2h}^{16} space group, it is possible to discriminate between all the permitted vibrational modes by choosing different Raman polarization configurations along single crystal samples. Defining a orthogonal tensor x, y and z, with z along the highest symmetry axes, A_g vibrational modes should be observed when the components of the polar tensor xx, yy, and zz are non-null, while contribution to B_{1g}, B_{2g} and B_{3g} modes should be given, respectively, from xy, yz, and xz components. From an experimental point of view, the condition is achieved by adequately choosing the geometrical and polarization configurations during the acquisition of the Raman spectrum. A_{1g} modes were measured in backscattering configuration by arranging the polarizer in parallel with the incident radiation, polarized along one of the three main axes, while B_{1g}, B_{2g}, and B_{3g} modes were obtained in backscattering configuration by switching the incident crystal face while arranging the polarizer in order to allow the transmission only of the non-parallel radiation. The independent exact scattering configurations obtained by polarizing the incident and scattered light along the principal crystal directions and the allowed phonon mode symmetries in each configuration can thus be measured. The results are shown in Table 1 and Fig. 3.

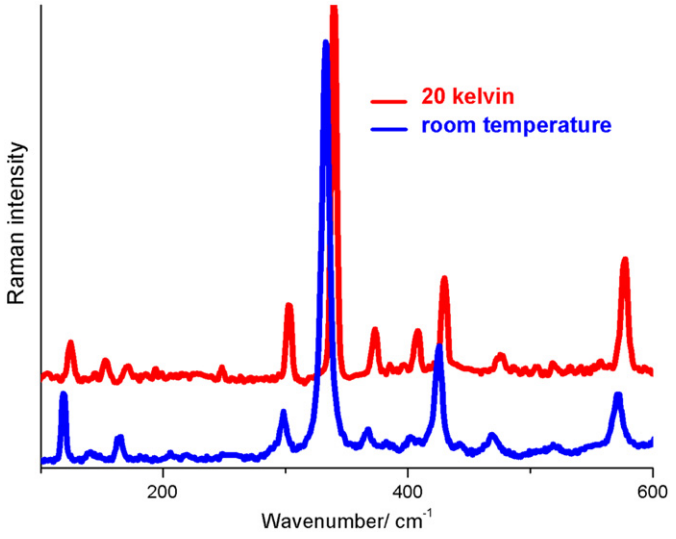

Fig. 2. Unpolarized Raman spectra of $LuAlO_3$ samples collected at low temperature (red line) and room temperature (blue line). (For interpretation of the references to color in this figure legend, the reader is referred to the web version of this article.)

The analysis of the measured spectra shows the presence of seven A_{1g} modes (117, 145, 295, 364 , 440, 550 and 571 cm^{-1}, respectively), two B_{1g} modes (299 and 401 cm^{-1}), four B_{2g} modes (164, 330, 424 and 569 cm^{-1}) and three B_{3g} modes (136, 465 and 550 cm^{-1}). The A_{1g}, B_{1g}, B_{2g} and B_{3g} vibrational modes of LuAP were assigned by confrontation with their vibrational correspondents in similar perovskites, particularly $YAlO_3$ (YAP) and the mixed compound $Lu_{0.7}Y_{0.3}AlO_3$ (LuYAP), as shown in Table 1 [24,25]. The occurrence of a varied population on one of the crystal sites allows to point out different shift effects caused by the presence of RE (lutetium in the present work) on A_{1g} ,$B_{1g,}$ B_{2g}, B_{3g} vibrational modes. In fact modes corresponding to A-site vibrations are not the only ones affected, as variations can be also registered for modes corresponding to vibrations of the AlO_6 octahedra. This evidence is particularly relevant in the case of the first B_{1g} vibrational mode, corresponding to an out-of-phase rotation of the AlO_6 octahedra, whose variation in position proportionally to the increasing presence of lutetium in the A site of the cell causes a blue-shift of approximately 40 cm^{-1} between YAP and LuAP crystals (from 258 to 299 cm^{-1}). This effect can be better observed from the analysis of Raman

Table 1
Raman peaks and vibrational modes of LuAP, YAP and LuYAP crystals.

YAP (cm^{-1})	LuYAP (cm^{-1})	LuAP (cm^{-1})	Vibrational modes	Assignment
144	123	117	A_{1g}	R(x)
187	177	136	B_{3g}	R(z)
190	190	145	A_{1g}	R(y)
217	196	164	B_{2g}	R(x)
258	280	299	B_{1g}	Out-of-phase rotations of AlO_6 around y
265	287	295	A_{1g}	In-phase rotations of AlO_6 octahedra around y
280	311	330	B_{2g}	O1(z)
336	357	364	A_{1g}	O1(x)
398	400	401	B_{1g}	In-phase rotations of AlO_6 octahedra around x
408	416	424	B_{2g}	Out-of-phase bending of AlO_6 octahedra
403	430	440	A_{1g}	Out-of-phase rotations of AlO_6 around x
462	458	–	B_{1g}	Out-of-phase stretching of AlO_6 in xz-planes
–	466	465	B_{3g}	Out-of-phase bending of AlO_6 octahedra
533	540	550	A_{1g}	Out-of-phase bending of AlO_6 octahedra
540	545	550	B_{3g}	Out-of-phase stretching of AlO_6 octahedra
544	555	569	B_{2g}	In-phase bending of AlO_6 octahedra
550	563	571	A_{1g}	In-phase stretching of AlO_6 in xz-planes

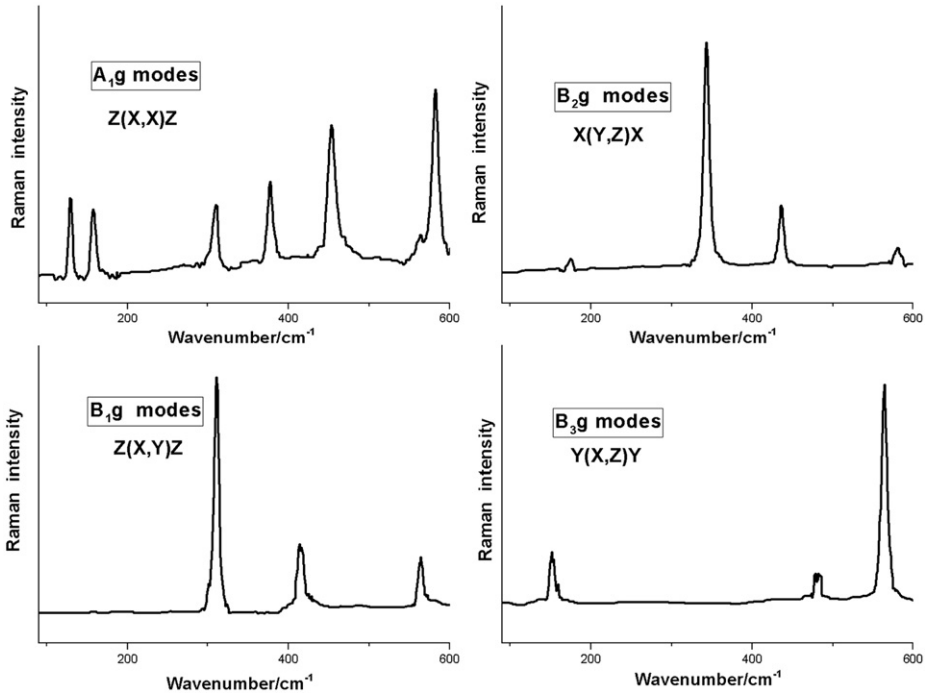

Fig. 3. LuAP Raman modes revealed through different geometries. Porto's notation has been used to describe the scattering geometry. The spectra were taken at room temperature on single crystal samples.

frequencies of the mixed compound LuYAP, whose vibrational peaks are always between the positions revealed for pure yttrium and lutetium perovskites (Table 1) [25].

A general analysis of the polarized spectra of LuAP in comparison with similar perovskites can help in stressing the differences and thus the role of the varying chemical elements in the general **A**–AlO_3 structure. The confrontation of analogous vibrational modes from LuAP, LuYAP and YAP allows the identification of different trends with the increasing substitution of lutetium over yttrium, resulting in both red-shifts and blue-shifts of the Raman modes, as previously observed in other mixed perovskites like $KMnF_3$ (Li, Na, Rb or Cs doped) [26] or $BaCe_xZr_{1-x}O_3$ [27], whose Raman modes positions are influenced by doping percentage.

In the low-energy region, where the peaks are caused by vibrational of rare earth in the *A* site (the region up to 295 cm^{-1} in the spectra of LuAP), the presence of Lu over Y causes an unambiguous downshift of the modes. On the other hand, two distinct classes of vibrations can be distinguished in the high energy region: Raman peaks due to rotations and bendings of the AlO_6 octahedra and vibration of oxygen atoms are present and overlapped in energy terms. These high-energy modes generally present a blue-shift proportionally to the presence of lutetium, although a couple of different trends can be pointed out.

In order to account for both the red- and blue-shifts, it is worth trying to comprehend the effects of the Lu/Y occupation of the *A* site from a structural point of view. The chemical element occupying the *A* site of the crystal structure directly influences the dimension of the body centered cuboctahedron: the substitution of Lu (having a smaller radius than Y) over Y determines a shrinking effect. Actually, similarly to orthorhombic rare-earth trifluorides (YF_3 and LnF_3) [28], both mass effects and the role of changings in the volume of the unit cell should be considered in order to understand the variations in phonon modes depending on the substitution process with heavier elements. While the low-frequency vibrations, depending mainly on the RE mass, downshift with increasing atomic number, most of high-frequency vibrations depend rather on the unit cell volume changes. A third group of modes present a competition between these two effects, so that their values do not change substantially.

In particular the shrinking of *A*-sites-polyhedra plays a far more important role in the variations of both types of higher energy vibrational modes, because its effect on oxygen and AlO_6 octahedra (formed around the central site of the lutetium polyhedra) vibrations can be considered analogous to external stress, whose expected effect is a shift towards higher wavenumbers of the Raman peaks. On the other hand, the faint red-shift observed for a B_{1g} and one B_{3g} modes relative to AlO_6 octahedra vibrations

Table 2
Fitting ranges and main results from the best fitting curves of LuAP EXAFS data collected at room temperature.

R range (Å)	1.1–4.0	***k* range ($Å^{-1}$)**	2.0–11.6	
***R* factor**	0.0086 (0.0023)	S_0^2	1.000 (0.008)	
Single scattering paths	**Model data**		**Room temperature data**	
	***R* eff (Å)**	***dR* (Å)**	***R* (Å)**	σ^2
Path 1: [O1_1]	2.223	0.033	2.25619	0.004 (2)
Path 2: [O2_1]	2.286	−0.106	2.18006	0.004 (2)
Path 3: [O1_2]	2.313	0.034	2.34711	0.004 (2)
Path 4: [O2_2]	2.448	0.036	2.4836	0.017 (3)
Path 5: [O2_3]	2.545	0.038	2.58274	0.017 (3)
Path 6: [O1_3]	2.943	0.043	2.9861	0.017 (3)
Path 7: [Al_1]	3.004	0.014	3.01739	0.005 (1)
Path 8: [Al_2]	3.100	0.014	3.11453	0.005 (1)
Path 9: [O1_4]	3.108	−0.144	2.96435	0.005 (1)
Path 10: [Al_3]	3.198	0.015	3.21248	0.005 (1)
Path 11: [O2_4]	3.216	−0.149	3.06765	0.005 (1)
Path 12: [Al_4]	3.467	0.127	3.59324	0.005 (1)
Path 13: [Lu1_1]	3.607	0.038	3.64543	0.005 (1)
Path 14: [Lu1_2]	3.695	0.111	3.8064	0.005 (1)
Path 15: [Lu1_3]	3.774	−0.023	3.75096	0.012 (6)

should be ascribed to a particular matching effect of two distinct contributions: the inhomogeneity observed in the shrink of the RE polyhedra is hinted by a inhomogeneous decrease of the b cell parameter, while on the other hand it is paired with a decrease in radius of the RE at the center of the AlO_6 octahedra. These factors can concur to reduced energies in vibrational modes.

The analysis of Raman spectra collected in the range 20–290 K was performed in order to see the dependence on temperature of the vibrational modes identified at room temperature, thus understanding the degree of distortion of the perovskite.

Fig. 2 reports the unpolarized Raman spectra of LuAP samples collected at 20 K and 290 K in the same scattering geometry. The comparison of these data shows two main variations caused by temperature. First, a rigid blue-shift of the peaks can be observed in the spectrum recorded at 20 K with respect to the one recorded at room temperature: this fact confirms that the lowering of temperature causes a shrinking of the crystal and a decrease in cell dimensions, which is in good accordance with a shift of the peaks towards high wavenumbers [29]. In second instance, a reduction in spectral width of Raman peaks collected at 20 K can be observed, hinting to the fact that mean phononic lifetime is mainly influenced by variations in temperature, as opposed to scattering due to reticular imperfections: this fact lead us to hypothesize a weak distortion of the perovskite crystal [30].

3.2. EXAFS measurements

LuAP was investigated by means of EXAFS spectroscopy in transmission mode at the L_3 absorption edge of lutetium. The spectra were collected at room temperature in order to assess the formation and characteristics of an orthorhombic perovskite (Table 2). The fitting procedures were carried out using the IFEFFIT package, which adapts a user-defined theoretical model (in our case a perovskite structure with sound $LuAlO_3$ cell parameters [2]) to the actual crystal structure obtained by EXFAS data analysis; indications on the goodness of the fit are given by the *R* factor. The detail of experimental analysis procedure is reported in the previous section. The region under analysis was a sphere centered at the absorption site (lutetium) and comprising the previously indicated shells up to the nearest Lu neighbors, in order to achieve results on the whole crystal cell. A set of fitting parameters was consequently chosen in order to assess each contribution, while trying to minimize their number for sake of

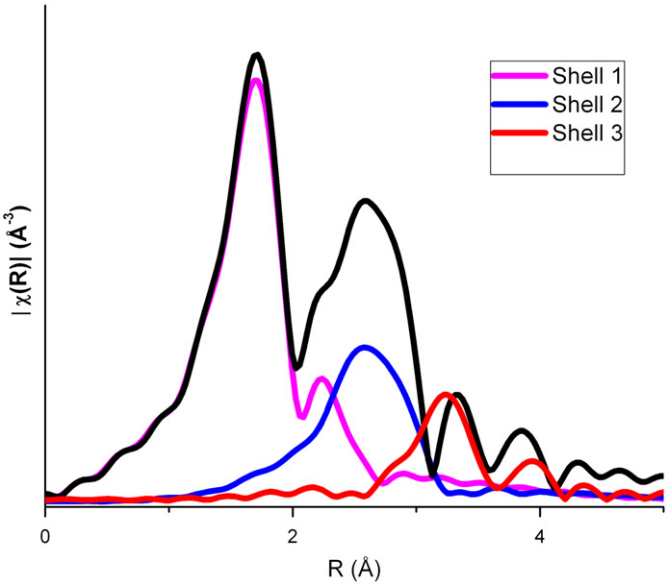

Fig. 4. R-Space EXAFS data (in black) and sum of fitted scattering paths for three radially distributed shells. Shell 1 (violet) features oxygen atoms, shell 2 (blue) features aluminum and oxygen atoms, shell 3 (red) features lutetium atoms. (For interpretation of the references to color in this figure legend, the reader is referred to the web version of this article.)

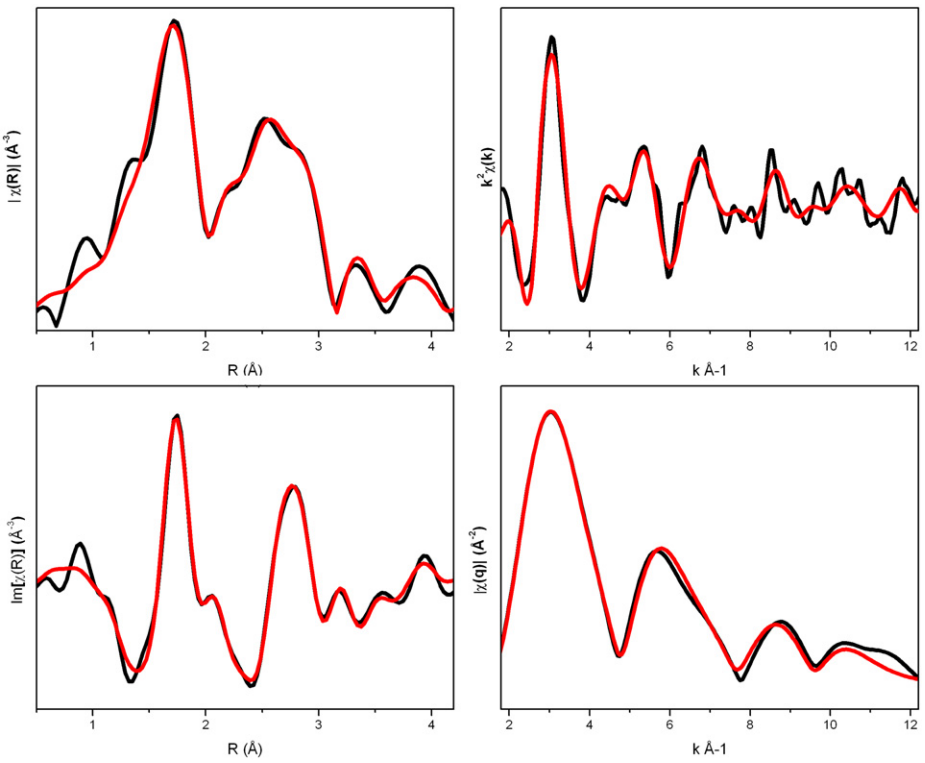

Fig. 5. EXAFS data (in black) and best fitting curves (red) of LuAP collected at room temperature at the L3 absorption edge of lutetium (9244 eV). (For interpretation of the references to color in this figure legend, the reader is referred to the web version of this article.)

goodness of calculations. Different parameters for scattering distances were chosen according to the elements involved and to the distance from the absorption site, while different σ^2 parameters indicated contributions at varying distances from the absorption site. The results of fitting procedures are shown in Figs. 4 and 5 and Table 2 and show the good agreement between theoretical model and experimental data. In particular, it is possible that the results of the analysis allow the assignment of peaks in the EXAFS spectrum to contributions from different "shells", as shown in Fig. 4.

The expectations concerning the formation of a distorted perovskite are satisfied, as proven also by variations in single scattering distances of the fitted structure in respect to the theoretical model. The occurrence of a degree of distortion in the structure is shown by the diverse variations of single scattering paths: differences in sign and magnitude of the dR parameter (adapting the theoretical R_{eff} scattering distance to experimental data) for paths of different "shells" exclude the possibility that variations in the fitted structure from the model could be solely caused by scale factors and should be attributed to distortions given by tilting of AlO_6 octahedra.

Bearing in mind the initial assumptions that cell dimensions are heavily related to *A* sites (in our case Lu), it is possible to estimate cell parameters with some basic geometrical calculations coming from the positions of lutetium atoms in the fitted structure. As a consequence, cell parameters at room temperature can be calculated as $a=5.11$ Å, $b=5.35$ Å, $c=7.52$ Å (205.51 Å^3), which are slightly oversized in respect to old literature data ($a=5.10$ Å, $b=5.33$ Å, $c=7.30$ Å [2], 198,43 Å^3). Bearing in mind that a pseudocubic lattice constant can be defined as $a=\sqrt[3]{1/4abc}$, the new cell parameters define a pseudocubic constant of $a=3.72$ Å, which is in good accordance with the pseudocubic value of $a=3.75$ Å obtained with the equation derived by Ubic [17] (the pseudocubic constant obtained by old literature data is $a=3.67$ Å).

4. Conclusions

$LuAlO_3$ crystals were analyzed by means of Raman and Extended X-Ray Absorption Fine Structure spectroscopy. In particular, polarized Raman spectroscopy was used to achieve a complete analysis of the vibrational modes of LuAP crystal in the temperature range of 20–290 K. The characterization of crystal structure was obtained by giving an assignment to every vibrational mode; the analysis of Raman spectra permits the identification of two spectral zones, each relative to the vibrations of different crystal sites, and related to the chemical elements forming the crystal: a low wavenumbers zone, homogeneously affected by variations in mass of the chemical elements, and a high wavenumbers zone, whose dependency on the radius of chemical elements is less straightforward. EXAFS spectroscopy was performed in transmission mode at the L_3 absorption edge of lutetium. The analysis, starting from literature data, allowed a direct measurement of local structural characteristics and parameters, thus permitting an estimate on the effective dimension of the lutetium perovskites unit cell. Moreover, structural evidences obtained by EXAFS analysis can be well compared with results obtained by Raman spectroscopy, thus giving an overall agreement over the characteristics of $LuAlO_3$. The informations thus gathered on can offer a useful addition in the framework of a full structural characterization of $LuAlO_3$.

Aknowledgments

The authors would like to thank Dr. Marcello Coreno and Dr. Monica de Simone for their help and support during EXAFS measurements, Dr. Luca Olivi and Dr. Andrea Cognigni from XAFS beamline of Elettra Synchrotron Radiation facility in Trieste for their prompt helpfulness.

References

[1] A. Lempicki, J. Glodo, Nucl. Instr. Meth. Phys. Res. A416 (1998) 333–344.
[2] P.D. Dernier, R.G. Maines, Mater. Res. Bull. 6 (1971) 430–440.
[3] C. Dujardin, C. Pedrini, D. Bouttet, W. Verweij, in: P. Dorenbos, C.W.E. van Eijk (Eds.), Proceedings of the International Conference on Inorganic Scintillators and their Applications SCINT'95, Delft University Press, Delft, 1996, pp. 336–339.
[4] M. Nikl, Meas. Sci. Technol. 17 (2006) R37.
[5] I.G. Valais, C.M. Michail, S.L. David, A. Konstantinidis, D.A. Cavouras, I.S. Kandarakis, G.S. Panayiotakis, IEEE Trans. Nucl. Sci. 55 (2008) 785.
[6] J.H. Jung, Y. Choi, Y.H. Chung, O. Devroede, M. Krieguer, P.B. Bruyndockx, S. Tavernier, Nucl. Instrum. Meth. A 571 (2007) 669.
[7] W. Drozdowski, A.J. Wojtowicz, T. Łukasiewicz, J. Kisielewski, Nucl. Instrum. Meth. A 562 (2006) 254.
[8] A. Wojtowicz, P. Szupryczynski, D. Wisniewski, J. Glodo, W. Drozdowski, Phys. Condens. Matter 13 (2001) 9599–961.
[9] M. Nikl, V.V. Laguta, A. Vedda, Phys. Status Solidi B 245 (9) (2008) 1701–1722.
[10] The first and the last letters outside the bracket represent the incident and the scattered direction respect to the crystal axes, assuming the *z* component parallel to the *c*-axis. The two letters inside the bracket represent the polarization direction of the incident and scattered beam, respectively. The "–" symbol indicates no polarization of the backscattered light: T.C. Damen, S.P.S. Porto, and B. Tell , Phys. Rev. 142 (1966), 579.
[11] J.J. Rehr, J. Mustre de Leon, S.I. Zabinsky, R.C. Albers, J. Am. Chem. Soc. 113 (1991) 5135.
[12] J. Mustre de Leon, J.J. Rehr, S.I. Zabinsky, R.C. Albers, Phys. Rev. B 44 (1991) 4146.
[13] A.F. Wells, Structural Inorganic Chemsitry, 5th edition, Oxford Science, New York, 1984.
[14] U. Muller, Inorganic Structural Chemistry, 2nd edition, , 2007.
[15] L.Q. Jiang, et al., JPSC 67 (2006) 1531.
[16] R.L. Moreira, A. Dias, JPSC 68 (2007) 1617.
[17] R. Ubic, J. Am. Ceram. Soc. 90 (2007) 3326.
[18] I.M. Reaney, D. Iddles, J. Am. Ceram. Soc. 89 (2006) 2063–2072.
[19] D.R. Lide, CRC Handbook of Chemistry and Physics 87th Edn., CRC Press.
[20] A.M. Glazer, Acta Cryst. B 28 (1972) 3384.
[21] R.W.G. Wychoff, Crystal Structure, Krieger, Florida, 1986.
[22] C. Carabatos-Nédelec, M. Oussaïd, K. Nitsch, J. Raman Spectrosc. 34/5 (2003) 388–393.
[23] M. Oussaïd, P. Becker, C. Carabatos-Nédelec, J. Raman Spectrosc. 31/6 (2000) 535–538.
[24] J. Suda, O. Kamishima, K. Hamaoka, I. Matsubara, T. Hattori, T. Sato, J. Phys Soc. Jpn. 72 (2003) 1418.
[25] A. Casu, P.C. Ricci, A. Anedda, J. Raman Spectrosc. 40/9 (2009) 1224–1228.
[26] J. Kapusta, Ph. Daniel, A. Ratuszna, J. Phys.: Condens. Matter 14 (2002) 5433–5544.
[27] C. Chemarin, N. Rosman, T. Pagnier, G. Lucazeau, J. Solid State Chem. 149 (298) (2000) 307.
[28] M.M. Lage, et al., J. Phys. Condens. Matter 16 (2004) 3207.
[29] B.A. Weinstein, R. Zallen, in: G.Gutherodta Cardona (Ed.), Light Scattering in Solids, vol. IV, Springer, Heidelberg, 1984, pp. 463–521.
[30] M.N. Iliev, M.V. Abrashev, H.-G. Lee, V.N. Popov, Y.Y. Sun, C. Thomsen, R.L. Meng, C.W. Chu, Phys. Rev. B 57 (1998) 2872.